Technical note: Evolution of convective boundary layer height estimated by Ka-band continuous millimeter wave radar at Wuhan in central China

Zirui Zhang[1,2,3] Kaiming Huang[1,2,3] Fan Yi[1,2,3] Wei Cheng[4] Fuchao Liu[1,2,3] Jian Zhang[5] and Yue Jia[6]

[1]School of Earth and Space Science and Technology, Wuhan University, Wuhan, China

[2] Key Laboratory of Geospace Environment and Geodesy, Ministry of Education, Wuhan, China

[3]State Observatory for Atmospheric Remote Sensing, Wuhan, China

[4]Beijing Institute of Applied Meteorology, Beijing, China

[5]School of Geophysics and Geomatics, China University of Geosciences, Wuhan, China

[6]NOAA Chemical Sciences Laboratory, Boulder, CO, USA

Email Address: hkm@whu.edu.cn

Zip code: 430072

Abstract. Using the vertical velocity (w) observed by a Ka-band millimeter wave cloud radar (MMCR) at Wuhan, we investigate the evolution of convective boundary layer height (CBLH) based on a specified threshold of vertical velocity variance (σ_w^2). The CBLHs from the MMCR w in the selected durations are compared with those estimated by the lidar range corrected signal (RCS) and radiosonde temperature based on different algorithms, showing good agreement with each other. Although these algorithms are on basis of different dynamic and thermodynamic effects, the diurnal evolution of CBLH from MMCR is generally consistent with that from lidar, except for a few hours post-sunrise and pre-sunset due to the influence of aerosol residual layer on the lidar RCS. Meanwhile, the CBLH from MMCR shows less variation in occurrence of sand and dust, and swifter response of thick clouds, relative to that from lidar. In this case, σ_w^2 of the MMCR w identifies the CBLH based on dynamic effect, which can accurately capture the diurnal evolution of CBLH compared with that from the change of long time-mixing aerosol concentration. The monthly and seasonal features of CBLH at Wuhan is revealed via the MMCR measurement. Hence, considering that the MMCR is capable of continuous observation in various weather conditions, the MMCR w with high resolution can be applied to monitoring the evolution of CBLH in different atmospheric conditions, which is helpful for improving our comprehensive understanding of CBL and dynamic processes in CBL.

1. **Introduction**

The planetary boundary layer (PBL) is located in the lower part of the troposphere, and is where the air-land (or air-sea) interaction takes place, thus the PBL is directly impacted by the surface forcings (Stull, 1988). Owing to the combined effects of friction, evaporation and transpiration, heat transfer, and pollutant emission, the PBL is characterized by complex dynamical processes, with the prominent turbulence features of vorticity and compressibility (Bernardini et al., 2012; Schneider, 2008). The height of PBL varies with

local time, ranging generally from a few tens of meters to a few kilometers at mid latitudes. Since the PBL regulates the exchange of momentum, moisture and mass between the ground and the free atmosphere (Mahrt, 1999; Holtslag and Nieuwstadt, 1986), the structure of PBL is an important input variable in numerical weather-prediction and climate models (Edwards et al., 2020).

The convective boundary layer (CBL) is a type of PBL driven primarily by convection, and the CBL height (CBLH) has a distinct daily cycle. Convective sources include heat transfer from the ground surface warmed by solar radiation, and radiative cooling-induced air sinking from the cloud top, thus the evolution of CBL is mainly dominated by surface sensible heat, which is significantly influenced by weather conditions, such as clouds, and humidity near the surface (Kwon et al., 2022; Ribeiro et al., 2018; Zhang et al. 2014). On a clear day, the CBLH rises after sunrise and reaches its maximum in the afternoon (LeMone et al., 2010; Grossman and Robert, 2005; Yates et al., 2001). When the CBL collapses after sunset, most of aerosol particles within the CBL are deposited into the nocturnal stable PBL due to the rapid weakening of convectively driven turbulence, and some particles are transformed into an aerosol residual layer. The residual layer descends gradually due to the sinking effect until it is mixed with the CBL driven by the next day's post-sunrise convection (Blay-Carreras et al., 2014; Heus et al., 2010; Tennekes and Driedonks, 1981). At the CBL top, moisture, aerosols and other chemical substances can be entrained to the free atmosphere, leading to an entrainment transition zone between the CBL and the free atmosphere (Franck et al., 2021; Liu et al., 2021; Brooks and Fowler, 2007). Hence, the CBL has an influence not only on the dispersion of surface emissions and pollutants (Kong and Yi, 2015; Pal et al., 2015; Stull, 1988), but also on the weather processes above it through the entrainment process (Guo et al., 2017; Brooks and Fowler, 2007; Neggers et al., 2004).

The observations of in situ radiosonde and remote sensing are extensively used to estimate the CBLH and its seasonal features. Radiosonde can obtain high-precision meteorological parameters, such as

69 temperature, humidity, horizontal wind and pressure, providing the possibility of estimating CBLH through
70 various algorithms (Seidel et al., 2010; Seibert, 2000). Typically, the vertical gradients of potential
71 temperature and water vapor (including relative humidity and specific humidity) are used to determine the
72 CBLH (Zhang et al., 2022; Guo et al., 2021; Dang et al., 2019; Liu and Liang, 2010; Seidel et al., 2010).
73 Additionally, the CBL top can be evaluated using the profiles of refractivity and bulk Richardson number
74 derived from the temperature, pressure, vapor pressure and horizontal wind data (Burgos-Cuevas et al., 2021;
75 Guo et al., 2016; Zhang et al., 2014; Seidel et al., 2012; Basha and Ratnam, 2009). These retrieval
76 algorithms provide insights into the features of CBL from the perspective of energy exchange, mass
77 transport, turbulent motion and effect on radio propagation. Even so, radiosonde faces a severe limitation in
78 capturing the clear development of CBL due to its conventional release schedule, which typically occurs
79 only twice a day.

80 In contrast to radiosonde, ground-based remote sensing offers high-temporal resolution in observational
81 profiles, which is essential to investigate the diurnal evolution of CBL. Wind profile radar can measure the
82 atmospheric wind speed and direction by analyzing the Doppler shift of the backscattered waves of multiple
83 beams (Liu et al., 2019; Singh et al., 2016; Seibert, 2000). The electromagnetic beams are reflected back due
84 mainly to the atmospheric refractive index change caused by the non-uniform vertical structure of the
85 atmosphere, such as vertical gradients in temperature, humidity, and turbulence, thus received echo and
86 retrieved wind from radar contain the information related to the atmospheric vertical structure. In this way,
87 several parameters from the wind profile radar measurement, such as signal-to-noise ratio, Doppler spectral
88 width, and refractive index structure constant, are utilized to retrieve the CBLH for every 30-60 minutes
89 based on their vertical gradients or chosen thresholds (Burgos-Cuevas et al., 2023; Bianco et al., 2022;
90 Solanki et al., 2021; Allabakash et al., 2017; Sandeep et al., 2014). Nevertheless, previous studies showed
91 that the top of CBL derived from the radar observation may be influenced by strong residual layer and

shallow or large entrainment zone (Sandeep et al., 2014; Bianco and Wilczak, 2002).

Lidar is regarded as a powerful detection equipment for capturing the CBL development due to its high sensitivity to echo signals from various atmospheric components. Its relatively short operating wavelength allows it to receive echoes backscattered not only from aerosol and cloud particles, but also from atmospheric molecules. Nevertheless, since Rayleigh scattering of atmospheric molecules is much weaker than Mie scattering of aerosol particles, the profile of lidar backscatter coefficient or range corrected signal (RCS) from aerosols is applied to determining the CBLH by tracing the height where the aerosol concentration sharply decreases with height. Accordingly, many techniques have been developed to identify the extreme value of RCS gradient (Liu et al., 2021; Su et al., 2020; Dang et al., 2019; Yang et al., 2017; Granados-Muñoz et al., 2012). As a simplified low-power lidar, ceilometer is initially designed to measure the height of cloud base, thus similarly, the backscatter profile in the ceilometer observation can be employed in the CBL investigation (Zhang et al., 2022; Schween et al., 2014; Van Der Kamp and McKendry, 2010). However, due to the incapability of lasers to penetrate clouds, the CBLH may be contaminated and even misinterpreted by clouds within the CBL in the lidar and ceilometer measurements (Schween et al., 2014).

With the advances in atmospheric sounding technology, the vertical velocity from Doppler lidar provides a direct estimation of CBLH, which can reduce the impact of strong aerosol concentration within the residual layer on the retrieved CBLH (Burgos-Cuevas et al., 2023; Dewani et al., 2023; Huang et al., 2017; Schween et al., 2014; Barlow et al., 2011). At the initial stage of CBL formation in the morning and the rapid decline stage of CBL in the late afternoon (Dewani et al., 2023; Manninen et al., 2018; Schween et al., 2014; Barlow et al., 2011), aerosol particles in the residual layer may cause the CBLH to be overestimated several hundred meters. This discrepancy is due to aerosols from a long time-mixing process rather than the current situation of convectively driven turbulence (Burgos-Cuevas et al., 2023; Schween et al., 2014;

115 Pearson et al., 2010). When utilizing Doppler lidar data, a specified threshold of vertical velocity variance is
116 used to define the height of CBL top. This method has been validated by comparison with the radiosonde
117 observation (Dang et al., 2019; Li et al. 2017; Granados-Muñoz et al., 2012), and the sensitivity of threshold
118 has been discussed across different sites (de Arruda et al., 2018; Manninen et al., 2018; Schween et al., 2014;
119 Barlow et al., 2011; Pearson et al., 2010). A disadvantage of lidar is that it has a large blind range and
120 incapability to penetrate clouds, thus because of that, it is valuable to utilize microwave cloud radar that
121 offers good low altitude coverage and superior performance in cloud penetration. In the cloud observation, a
122 weak echo layer always exists near the surface, from which the vertical velocity can be retrieved. However,
123 there are few reports utilizing vertical velocity obtained from Doppler cloud radar for the CBL
124 investigations.

125 In present study, we estimate the CBLH based on the vertical velocity from a Ka-band millimeter wave
126 cloud radar (MMCR) at Wuhan, and compared this result with that derived from the lidar RCS by three
127 algorithms, and from radiosonde data by two algorithms. These algorithms are on basis of different dynamic
128 and thermodynamic effects, respectively, thus the comparison enhances our comprehensive understanding of
129 CBL and retrieval algorithms. Then, the general features of monthly and seasonal mean CBLHs are studied
130 by using the MMCR observation with high-temporal resolution. In section 2, the MMCR, lidar and their
131 data are briefly described. In Section 3, we discuss the methods that are used to identify the CBL top from
132 the MMCR, lidar and radiosonde measurements. In section 4, we present four examples of CBLH diurnal
133 evolution in different seasons by comparing the CBL tops retrieved from the MMCR and lidar
134 measurements, and then investigate the monthly and seasonal mean CBLHs over Wuhan in Section 5.
135 Section 6 provides a summary.
136

137 **2. Instruments and Data**

In this study, the CBLH derived from the MMCR measurements is compared with that from the lidar measurements. The Ka-band MMCR and lidar are situated at the Atmospheric Remote Sensing Observatory (ARSO) in Wuhan University (WHU, 30.5°N, 114.4°E). Wuhan, an inland megacity in central China, is located in the east of Jianghan Plain, with a resident population of over 12 million. The climate of the city is humid, dominated by the subtropical monsoon, which is characterized by abundant precipitation and four distinct seasons (Guo et al., 2023). Due to heavy traffic and industrial activities, large amounts of aerosols are emitted from the industrialized metropolis. Sandstorms from the northwest often pass through Wuhan, especially in spring. These sandstorms cause the remarkable variation in the spatial distribution and concentration of aerosols. Frequent sand and dust activity along with cloudy weather poses significant challenges for the Ka-band MMCR and lidar in accurately capturing the CBL evolution.

2.1 Ka-Band Radar

The WHU-CW MMCR established by the ARSO adopted a continuous wave (CW) system, and is a Ka-band frequency-modulated continuous wave (FMCW) Doppler radar. The MMCR is installed in WHU, as shown in Figure 1. The radar system transmits a mean power of 50 W at operating frequency of 35.035 GHz through 0.38° width beam formed by a Cassegrain antenna with 1.5 m diameter. Backscatter echoes from aerosol and cloud particles are received by the other same Cassegrain antenna, and then are sent to the signal processing subsystem to obtain the radial distribution of parameters that represent the characteristics and motion of particles, such as reflectivity factor, Doppler velocity, and Doppler spectrum width. Because of almost continuous transmitting and receiving, FMCW radar has generally a much higher mean power relative to pulse radar, which improves the capacity of MMCR to detect weak echo targets. Meanwhile, by modulating and demodulating the continuous wave, the FMCW radar measurement has an adjustable range and time resolution. In non-precipitation, the MMCR measurement has a temporal resolution of 0.26 s and a maximum measurable velocity of 4.30 m s^{-1} without aliasing effect, which are adjusted to be 0.104 s and

10.75 m s^{-1} in precipitation as the size and falling speed of hydrometeors increase (Mao et al., 2023), respectively. The MMCR observation has been applied to the investigations of cloud and precipitation over Wuhan in previous works (Fang et al., 2023; Mao et al., 2023).

The MMCR has a maximum detectable distance of about 30 km and a sensitivity of -30 dBZ at the distance of 10 km. In the MMCR measurement, there are weak echoes generally less than -40 dBz within a few kilometers above the surface. The weak echoes near the surface are attributed to the backscattering of small insects and aerial plankton in some studies (Franck et al., 2021; Chandra et al., 2010; Achtemeier, 1991), and are also suggested to come from the scattering of dust particles in other studies (Görsdorf et al., 2015; Clothiaux et al, 2000; Moran et al., 1998). Considering that the size of large dust particles, plant aerosol particles, and aerosol particles from combustion can be much larger than 10 μm, it is possible for the large aerosol particles to cause these weak echoes observed by MMCR. The servo-mechanical subsystem conducts the MMCR to work in specified directional mode or scanning mode. In 2020, the MMCR was operated in the vertical pointing mode, and the observation is recorded with a vertical resolution of 30 m. In this study, we attempt to explore the CBL evolution at Wuhan from the Ka-band MMCR observation in 2020.

2.2 Polarization Lidar

The WHU-PL polarization lidar developed by the ARSO is also located in WHU, about 0.5 km from the Ka-band MMCR. The lidar telescope is 70 m above sea level, which is about 30 m higher than the MMCR antenna. Expanded laser beam overlaps with the full view field of the receiving telescope at a height of 0.3 km, thus this height is the low limit of lidar detection. The lidar data has a temporal resolution of 1 min, and the same vertical resolution of 30 m as the MMCR data. In this study, we regard the height of MMCR antenna as a baseline, and then the initial height of lidar data is set at 0.33 km.

The lidar system consists of transmitting subsystem receiving subsystem and information processing

subsystem. The lidar vertically emits the laser pulses of 120 mJ at operating wavelength of 532 nm with a repetition rate of 20 Hz by a frequency-doubled Nd: YAG laser. The output polarized laser beam has a fine polarization purity with depolarization ratio less than 1:10000 by using a Brewster polarizer. Light backscattered by aerosol and cloud particles and atmospheric molecules is collected by a telescope with 0.3 m diameter. After separated through an interference filter with 0.3 nm bandwidth centered at 532 nm, the elastically backscattered light is incident on a polarization beam splitter prism, and then the two-channel polarized light are focused onto two photomultiplier tubes (PMTs), respectively. The signals from the two PMTs are transferred to a personal computer (PC)-controlled two-channel transient digitizer, which can obtain the echo signal intensity and volume depolarization ratio through the PC processing. Backscatter coefficient is retrieved based on the backward iteration algorithm under the condition of a given lidar ratio proposed by Fernald and Klett (Fernald, 1984; Klett, 1981), and then the RCS is derived from the backscatter coefficient (Freudenthaler et al., 2009; Immler and Schrems, 2003). The lidar configuration and depolarization comparison with the measurement from the cloud-aerosol lidar and infrared pathfinder satellite observation (CALIPSO) were in detail described in the early study (Kong and Yi, 2015).

3. Methodology

Given that the CBLH is estimated from instruments that retrieve different variables, the algorithms that are utilized to make such estimations are also based on different principles, which are explained in the following subsections.

3.1 Gradient, Variance and Wavelet Transformation Methods

In the lidar observation, the CBLH is derived from the RCS, which is approximately proportional to the aerosol concentration (Kong and Yi, 2015; Lewis et al., 2013; Pal et al., 2010; Emeis et al., 2008). Generally, aerosols are well-mixed within the CBL due to the convectively driven turbulence, and its concentration

decays sharply over the CBL top. Hence, the gradient (Grd) method is often utilized to investigate the CBLH by identifying the strongest or minimum gradient of RCS. The wavelet covariance transformation (WCT) method, with a chosen Harr wavelet function, estimates the CBL top by investigating the correlation of the RCS variation with a step function (Zhang et al., 2021; Angelini and Gobbi, 2014; Pal et al., 2010; Baars et al., 2008; Brooks, 2003). Essentially, the WCT method can be considered as a smooth enhancement of Grd method, which may be less affected by noise than the Grd method (Davis et al., 2000; Baars et al. al., 2008).

On the other hand, because of the entrainment process, there is a frequent exchange of matter and energy between the CBL and the free atmosphere, causing the dramatic variation of aerosol concentration or lidar RCS on small time scales around the CBL top (Zhang et al., 2018; Kong and Yi, 2015). In this case, the variance (Var) method is used to determine the CBL top by identifying the maximum variance of RCS during a relatively long period (Lammert and Bösenberg, 2006; Martucci et al., 2004; Piironen and Eloranta, 1995). We estimate the CBLH from the lidar RCS in a period of 30 min by using the three methods, for instance, the CBLH at 12:00 LT (the same below) is calculated based on the RCS data from 11:45 to 12:15.

3.2 Threshold Method

The variance (σ_w^2) of vertical velocity (w) is representative of the level of turbulent activity, thus a threshold of σ_w^2 is applied to determining the CBLH in the Doppler lidar measurement. The threshold is chosen to be 0.04 $m^2 s^{-2}$ in the regions with weak turbulence (Tucker et al., 2009), 0.3 $m^2 s^{-2}$ in a tropical rainforest (Pearson et al., 2010), and 0.4 $m^2 s^{-2}$ in the regions with central European climate (Schween et al., 2014; Träumner et al., 2011), while the thresholds of 0.1 and 0.2 $m^2 s^{-2}$ are selected in the urban landscapes since the retrieved CBLH is not heavily dependent on the given thresholds (Burgos-Cuevas et al., 2023; Huang et al. 2017; Barlow et al., 2011). Similarly, the threshold method is also used to determine a CBLH from the more than 6000 w profiles in the MMCR measurement during a period of 30 min.

Figure 2 presents the distribution of w from the Ka-band MMCR observation and RCS (in arbitrary unit) from the lidar measurement on 15 August 2020. The day is 3 days later than the rainy day of 12 August. By taking observations for a period of 30 min from 11:45 to 12:15, we calculate the mean w and RCS, and estimate the position of CBL top by means of different algorithms, which are shown in Figure 3. From the lidar RCS, the CBLH is 1.35 km in the Grd and WCT methods, and 1.32 km in the Var method. In the MMCR observation, σ_w^2 has a clear downward trend with increasing height, with the values of about 1.36 $m^2 s^{-2}$ from the near ground to 0.15 $m^2 s^{-2}$ at 1.47 km, and then maintains slight fluctuations around the value of 0.15 $m^2 s^{-2}$ to higher altitudes. For a specified threshold of 0.3 $m^2 s^{-2}$, the CBL top is identified at the height of 1.35 km, which is in agreement with the lidar results.

It can be noted from Figures 3d and 3f that the CBLHs in the mean RCS profile are around the position with the most rapid change, while the CBLH retrieved from the MMCR σ_w^2 is not related to the vertical variation of mean w. σ_w^2 indicates the turbulence level under the current condition, whereas, RCS tends to reflect the variation in the concentration of long time-mixing aerosol particles caused by dynamic effects (Kotthaus et al., 2023). Hence, the threshold method is a dynamical algorithm, which is more effective in capturing the dynamic changes within the CBL compared to the aerosol concentration algorithm based on the lidar RCS. In this way, the MMCR observes the high-temporal resolution data of w, making it available for analyzing diurnal evolution of CBL in different months and seasons. However, based on earlier studies, the selected threshold values are subject to change across the different regions (Burgos-Cuevas et al., 2023; Schween et al., 2014; Pearson et al., 2010; Tucker et al., 2009).

In Figure 3e, σ_w^2 decreases quickly from 0.4 $m^2 s^{-2}$ at 1.29 km to 0.15 $m^2 s^{-2}$ at 1.47 km, indicating that the CBH top at noon is less sensitive to the selected threshold within 0.15-0.4 $m^2 s^{-2}$. Figure 4 depicts the CBLHs on 15 August 2020 at the thresholds from 0.2 to 0.45 $m^2 s^{-2}$. Nevertheless, the CBLH from 09:30 to 17:30 remains relatively stable with little change at the different thresholds, and the discrepancy among

these thresholds arises mainly in the initial growing and final decaying stages of CBL.

σ_w^2 of MMCR w determines the CBL top from the perspective of dynamic effect, and the CBLH can be estimated from the temperature data based on the thermodynamic effect. Here, we compare the CBLH derived from the MMCR w with that from the radiosonde data. Radiosonde is typically launched in Wuhan at 08:00 and 20:00. Given that the sun has set by 20:00, we present the comparison at 08:00. The radiosonde data are provided by University of Wyoming from the website at https://weather.uwyo.edu/upperair/bufrraob.shtml. The vertical resolution of radiosonde data in Wuhan was approximately 0.5-1.0 km before June 2021, and then was improved to a range of tens to hundreds of meters at higher altitudes. Therefore, we select the high-resolution data in the days without precipitation for our analysis.

We estimate the CBLH from the radiosonde data by using the methods of potential temperature (θ) gradient and bulk Richardson number (Ri) threshold. The potential temperature gradient (Grd_θ) is calculated at two adjacent heights in the radiosonde data, and the CBLH is determined by the maximum gradient in the profile of Grd_θ (Seidel et al., 2010). The bulk Richardson number is expressed (Zhang et al., 2014; Seibert et al., 2000), as follows,

$$Ri(z) = \frac{(g/\theta_{vs})(\theta_{vz} - \theta_{vs})z}{(u_z - u_s)^2 + (v_z - v_s)^2 + (bu_*^2)} \quad (1)$$

where g is the acceleration due to gravity; z is the height; θ_v is the virtual potential temperature; u_* is the surface friction velocity; u and v are the zonal and meridional wind components, respectively; and b is a constant, which is usually set to zero due to the fact that friction velocity is much weaker compared with the horizontal wind (Seidel et al., 2012). The subscripts of z and s denote the parameters at z height and surface level, respectively. In the profile of Ri, the CBLH is identified when Ri firstly crosses a threshold value upward from the ground, and the threshold is typically taken as 0.25 in early studies (Guo

et al., 2021; Seibert et al., 2000), which is chosen in the analysis.

Figure 5 shows the comparisons of CBLHs derived from the MMCR and radiosonde measurements at 8:00 on 21 and 25, July 2021, respectively. On 21, for a threshold of σ_w^2=0.3 $m^2 s^{-2}$, the CBLH of 0.39 km from the MMCR w is in agreement with that of 0.40 km from the radiosonde Grd_θ, which are slightly larger than that of 0.34 km from the radiosonde Ri. In contrast to this, on 25, the CBLH is 0.57 km from the MMCR w, which is consistent with that of 0.59 km from the radiosonde Ri, but is slightly higher than that of 0.45 km from the radiosonde Grd_θ. Nevertheless, in the whole, the results from all the three methods roughly agree with each other.

Figure 6 displays the scatterplot of CBLHs identified by the MMCR w, and the radiosonde Grd_θ and Ri at 8:00 on the clear days in June and July 2021. The different variables and algorithms are used in the three methods, thus there are some differences of CBLHs derived from these methods, as shown in Figure 6. The CBLH from σ_w^2 of MMCR w has the correlation coefficients of 0.83 and 0.81 with that from the radiosonde Grd_θ and Ri, respectively, which are highly consistent with the correlation coefficient of 0.83 from the radiosonde Grd_θ and Ri. These results support the threshold of σ_w^2= 0.3 $m^2 s^{-2}$ applied to the CBLH estimation in Wuhan. In following analysis, we take 0.3 $m^2 s^{-2}$ as the threshold to determine the CBLH in the MMCR observation.

It can be noted that the comparison focuses solely on the CBLH at 8:00 rather than the diurnal evolution of CBLH, owing to the lack of radiosonde observation. Consequently, we analyze the diurnal evolution of CBLH derived from the MMCR and lidar measurements.

4. Case Investigation and Comparison

Figure 7 presents the CBLH evolution on 15 August 2020 from the lidar RCS based on the Grd, Var and WCT methods, and the comparison with that obtained from the MMCR σ_w^2, together with the distribution

298 of MMCR reflectivity factor in the range of 10-15 km. As shown in Figure 7c, due to the influence of
299 aerosol residual layer, the CBLH from the lidar RCS fluctuates from about 1.56 km at 06:00 down to 1.17
300 km at 09:30, however, with the sunrise at 05:50, the CBL top derived from the MMCR σ_w^2 gradually rises
301 from about 0.09 km at 06:00 to 1.17 km at 09:30. It is interesting that the CBLH from the lidar RCS
302 variance drops at 07:30 and then shows a change similar to that from the MMCR σ_w^2. Both the variances of
303 w and RCS represent the deviation degree of their small time scale values relative to their 30 min-mean
304 values, which may be responsible for the similar results. When the CBL ascends gradually and mixes with
305 the residual layer, the CBLHs in the lidar and MMCR observations are consistent with each other between
306 09:30 and 17:00, including a slight drop at 12:30 and 14:30 (from the gradient and variance of RCS). The
307 maximum height of CBL is about 1.71 km at 14:00 and 15:00 based on σ_w^2 and the RCS gradient and
308 variance.

309 One can note from the reflectivity factor distribution in Figure 7b that cirrus clouds occur from 17:00,
310 develop rapidly into the thick clouds at about 11-14.4 km at 17:30, and then dissipate quickly after 17:30. In
311 the MMCR observation, the CBLH shows an obvious reduction between 17:30 and 18:30, and then a lift as
312 the clouds dissipates rapidly. Earlier studies from the Doppler lidar w investigated the complex influence
313 of low-level clouds on the CBL and turbulence. The cloud-top radiative cooling drives top-down convective
314 mixing, leading to the increasement of σ_w^2 (Hogan et al., 2009; Harvey et al., 2013; Manninen et al., 2018).
315 Whereas, during the warm season, the magnitude of σ_w^2 from the lidar w is large on clear-sky days and
316 decreases on cloud-topped days, and the intensity of turbulence reduces with an increase in the cloud
317 fraction within the CBL, except in the cloud layer that exceeds 90% of the CBL thickness (Dewani et al.,
318 2023). Here, the cirrus clouds are above 11 km, thus the cloud-top driven convective mixing has little impact
319 on the low atmosphere, however, the thick clouds cool the surface by attenuating solar radiation, which can
320 weaken the surface-driven convective mixing. Therefore, the thick cirrus makes a large contribution to the

evident reduction of CBLH. The phenomenon of CBLH reduction also arises in the lidar RCS, especially from the RCS variance, but with a time lag due to the influence of a long time-mixing process on the aerosol distribution (Burgos-Cuevas et al., 2023; Schween et al., 2014). After the sunset at 19:05, the CBLH retrieved by σ_w^2 drops quickly to 0.27 km at 20:00 from 1.47 km at 19:00, while the top of aerosol residual layer (or horizontally migrating aerosol layer) identified by the lidar stays at a far higher level, especially from the RCS gradient and WCT.

Next, we select the observations on 31 January, 12 November, and 19 March 2020 to compare the CBLH evolutions. The three days, without clouds and precipitation, are chosen as the representative in different seasons. Figure 8 shows the CBLHs on 31 January derived from the four methods above, which are overlaid on the MMCR w and σ_w^2 and the lidar RCS, respectively. January is the coldest month of the year, and on 31 January, the minimum (maximum) temperature is -5 °C (4 °C) recorded in the weather forecast. Owing to the convection inhibited largely by the frigid surface and air, σ_w^2 shows that the CBLH develops very slowly upward to 0.3 km at 11:30 from 0.12 km at 07:30 as the sun rises at 07:15. Thereafter, the top of CBL escalates quickly to 0.9 km at 13:30, and reaches the maximum height of 0.99 km at 14:30, and during this period, the CBLH from the lidar RCS experiences a similarly rapid uplift, and attains the peak of 1.2 km at 14:00 from the RCS gradient and variance, and 1.14 km at 14:30 from the RCS WCT. In addition, it can be seen from Figure 8d that all the CBLHs from the lidar RCS are slightly larger than those from the MMCR σ_w^2, which may be attributed to the long time-mixing aerosols and wet surface in winter. After 14:30, the CBLH from σ_w^2 descends gradually, and approaches the ground at 17:30 prior to the sunset at 17:57, while at the sunset, the CBL top from the RCS is at 0.8-0.9 km due to the long time-mixing processes.

Figure 9 presents the CBLHs determined from the MMCR and lidar observations on 12 November 2020. With the sunset on this day in late autumn, the CBLH identified from σ_w^2 displays a little fluctuation until

10:30. After then, the CBL is rapidly developed to 0.51 km at 11:30, and mixes fully with the residual layer retrieved from the lidar RCS, thus the CBL tops have approximately the same evolution between the MMCR and lidar observations from 11:30 to 17:30, with the maximum values of about 0.75-0.78 km at 15:00 and 16:00. As the sun goes down at 17:27, the CBL from σ_w^2 rapidly shrinks close to the ground at 18:00, and aerosol particles left in the air form a residual layer, similar to the two cases above.

Figure 10 depicts the CBLH variations in the MMCR and lidar observations on 19 March 2020, together with the depolarization ratio from the lidar. In spring, sand and dust with different intensities from the northwest of China pass frequently through Wuhan. On this day, there is a fine sand and dust layer mostly above 1.8 km, with the depolarization ratios of about 0.08-0.12 in Figure 10c, which can also be noted from the distribution of w in the MMCR observation. Meanwhile, another sand and dust layer with the larger depolarization ratios of about 0.14-0.16 passes through Wuhan from about 14:00, and mixes with the lower part of the first sand and dust layer. In this situation, the MMCR observation indicates that the CBL starts to develop gently upward from the sunrise, and the upward trend of CBLH is also presented in the lidar measurement, but at higher altitudes. At 09:30, the CBLH is about 0.48 km in both the MMCR and lidar observations, and then rises steadily to 1.32 km at 16:00 and 16:30, showing a good agreement between the two observations. Subsequently, the CBLH from σ_w^2 undergoes two rapid declines. One occurs from 1.2 km at 17:00 to 0.51 km at 18:00, which is probably related to the sand and dust deposition in addition to the diminished radiation in the late afternoon, and the other arises after the sunset. However, because of the effect of sand and dust, the CBLH from the lidar RCS increases slightly from 1.32 km at 16:30 to about 1.38 km at 18:00 and 18:30, and then decreases gradually with time.

The CBLH is identified by the spatial and temporal variation of aerosol concentration from the lidar measurement and by the temporal change of w from the MMCR observation. The four examples demonstrate that except for the periods with the influence of aerosol residual layer, particularly during the

few hours after sunrise and before sunset, the MMCR CBLHs are generally in agreement with the lidar CBLHs. The residual layer causes a higher CBLH estimated by the lidar RCS than by the MMCR w because σ_w^2 is less contaminated by the residual layer relative to the aerosol concentration. Additionally, the CBLH estimated by σ_w^2 shows a rapid response to thick high-level clouds and less influence by the long-range transport of sand and dust. Hence, the MMCR observation can accurately retrieve the CBLH and capture its diurnal evolution, especially for the CBL in the blind range of lidar.

5. Monthly and Seasonal Mean CBLHs

To reveal the general characteristics of CBLH diurnal evolution in different months and seasons, we calculate the monthly and seasonal mean CBLHs by using the MMCR w on these days without precipitation in 2020. We consider that winter covers the months of December, January and February, while March, April and May are spring, June, July and August are summer and the rest is autumn.

Figure 11 illustrates the averaged CBLHs with the standard deviations superimposed on the mean σ_w^2 in each month and season. As the spot of direct sunlight slowly moves northward, the mean variance gradually increases from January to July, and then decreases gradually from August to December, moreover, the coverage height and time duration of its large values show an analogous monthly variation. In this case, the peak height of CBL ascends steadily from 0.66 km in January to 1.47 (1.44) km in July (August), and subsequently, descends gradually to the lowest height of 0.42 km in December. Additionally, at Wuhan, the plum rain starts in June and prevails in July. As shown in Figure 11, the CBLH in July has the largest standard deviation (between 13:00 and 19:00), which is possibly attributable to the cloudy and rainy weather besides the strongest radiation.

As for seasonal variation, as we expected, the mean σ_w^2 is the strongest in summer and the weakest in winter. Interestingly, the variance is significantly larger in spring than in autumn. Not only the maximum

CBLH of 1.14 km at 13:30 in spring is much higher than that of about 0.66 km at 13:30 and 14:00 in autumn, but also the mean σ_w^2 of 0.42 $m^2 s^{-2}$ in the CBL during spring is stronger than that of 0.35 $m^2 s^{-2}$ during autumn. The maximum height of CBL is 1.29 km at 14:30 and 15:00 in summer, and about 0.6 km at 14:30 in winter. In summer, the CBLH displays a feature of quick descent near twilight, and in autumn, the CBL shows a wider envelope with an earlier development and a later dissipation relative to that in winter though their maximum CBLHs are almost the same. In previous studies, based on the threshold of σ_w^2 from the Doppler lidar measurement in Mexico City (19.3° N, 99.1° E), the CBLH is higher in spring and summer, and lower in winter, while the maximum CBLH of about 1.5 km occurs in May, which is because the CBLH is suppressed to some extend by increased cloud cover in the rainy season between June and September (Burgos-Cuevas et al., 2021). However, the CBLH retrieved from the ceilometer backscatter data is obviously larger than that from the threshold of σ_w^2 (Burgos-Cuevas et al., 2021; Tang et al., 2016). Similarly, in the estimation of CBLH from the lidar RCS over Wuhan and Granada (37.18° N, 3.60° E), the maximum values of seasonal mean CBLHs in all the seasons are larger than those in our results although the gradual ascent of CBLH from winter and autumn to spring and summer is consistent with that in our results (Kong and Yi, 2015; Granados-Muñoz et al., 2012).

6. Summary

In this study, we estimate the CBLH from the profile of w in the Ka-MMCR observation by using a threshold of σ_w^2. The CBLH from MMCR is compared with that from the lidar RCS by utilizing the gradient, variance and wavelet methods, and from radiosonde data by using the methods of θ gradient and Ri, which demonstrates the general agreement of CBLH estimation based on different dynamic and thermodynamic effects. Then, we investigate the diurnal evolution of monthly and seasonal mean CBLHs based on the MMCR observation.

Although the RCS is proportional to aerosol concentration and w represents the vertical motion of aerosol particles, the comparison of four examples in different seasons indicates that the diurnal evolution of CBLH from the MMCR w is consistent with those from the lidar RCS, except for the initial growth and final decay phases. The discrepancy can mainly be attributed to the aerosol residual layer and the lidar blind range. The influence of residual layer on the lidar RCS generally causes an overestimation of CBLH, meanwhile, it is impossible for lidar to capture the CBL top within its large blind range. In addition, the CBLH in the MMCR observation shows less contamination by the long-range transport of sand and dust, and thick high-level clouds due to the rapid response of aerosol w relative to its concentration. In this case, the MMCR observation can capture the diurnal evolution of CBLH.

Using the profile of w from the MMCR observation on these days without precipitation in 2020, we investigate the diurnal evolution of monthly and seasonal mean CBLHs. The maximum value of monthly mean CBLH increases gradually from 0.66 km in January to 1.47 (1.44) km in July (August), and then decreases to the lowest height of 0.42 km in December. As for the seasonal behavior, the mean CBLH has the maximum heights of 1.29 km at 14:30 and 15:00 in summer, 1.14 km at 13:30 in spring, 0.66 km at 13:30 and 14:00 in autumn, and 0.6 km at 14:30 in winter. In addition, the statistical standard deviations are monthly-dependent, indicating that the CBLH is not only mainly regulated by the surface heating associated with solar radiation, but also significantly affected by weather conditions, such as humidity and clouds. Therefore, since the Ka-band MMCR is a powerful instrument for observing clouds and weak precipitation, the full-time MMCR observation with low blind height can obtain the entire diurnal evolution of CBLH, which helps us gain an insight into CBL features and also provides important input variables for weather prediction and climate models.

Code availability. Software code to obtain the results is available upon request from the corresponding author.

Data availability. All data used are available upon request from the corresponding author.

Author contributions. KH and FY conceptualized this study. ZZ and KH completed the analysis and the manuscript. WC, FL, JZ, YJ, and FY discussed the results and finalized the manuscript.

Competing interests. The authors declare that they have no conflict of interest.

Financial support. This work was supported by the National Key Research and Development Program of China (2022YFF0503700 and 2022YFB3901800) and the National Natural Science Foundation of China (42174189).

Acknowledgements.

We are grateful to the editor and reviewers for their valuable comments on our manuscript, and University of Wyoming for providing the radiosonde data at the website of https://weather.uwyo.edu/upperair/bufrraob.shtml.

References

Allabakash, S., Yasodha, P., Bianco, L., Venkatramana Reddy, S., Srinivasulu, P., and Lim, S.: Improved boundary layer height measurement using a fuzzy logic method: Diurnal and seasonal variabilities of the convective boundary layer over a tropical station, J. Geophys. Res.-Atmos., 122, 9211–9232, https://doi.org/10.1002/2017JD027615, 2017.

Achtemeier, G. L.: The use of insects as tracers for “Clear-Air” boundary-layer sturdies by doppler radar, J. Atmos. Ocean. Tech., 8, 746-765, https://doi.org/10.1175/1520-0426(1991)008<0746:TUOIAT>2.0.CO;2, 1991.

Baars, H., Ansmann, A., Engelmann, R., and Althausen, D.: Continuous monitoring of the boundary-layer top with lidar, Atmos. Chem. Phys., https://doi.org/10.5194/acp-8-7281-2008, 2008.

Barlow, J. F., Dunbar, T. M., Nemitz, E. G., Wood, C. R., Gallagher, M. W., Davies, F., O'Connor, E., and Harrison, R. M.: Boundary layer dynamics over London, UK, as observed using Doppler lidar during REPARTEE-II, Atmos. Chem. Phys., 11, 2111–2125, https://doi.org/10.5194/acp-11-2111-2011, 2011.

Basha, G. and Ratnam, M. V.: Identification of atmospheric boundary layer height over a tropical station using high-resolution radiosonde refractivity profiles: Comparison with GPS radio occultation measurements, J. Geophys. Res.-Atmos., 114, 2008JD011692, https://doi.org/10.1029/2008JD011692, 2009.

Bernardini, M., Pirozzoli, S., and Orlandi, P.: Compressibility effects on roughness-induced boundary layer transition, Int. J. Heat Fluid Fl., 35, 45–51, https://doi.org/10.1016/j.ijheatfluidflow.2012.02.007, 2012.

Bianco, L. and Wilczak, J. M.: Convective boundary layer depth: Improved measurement by doppler radar wind profiler using fuzzy logic methods, J. Atmos. Ocean. Tech., 19, 1745–1758, https://doi.org/10.1175/1520-0426(2002)019<1745:CBLDIM>2.0.CO;2, 2002.

Bianco, L., Muradyan, P., Djalalova, I., Wilczak, J. M., Olson, J. B., Kenyon, J. S., Kotamarthi, R., Lantz, K., Long, C. N., and Turner, D. D.: Comparison of observations and predictions of daytime planetary-boundary-layer heights and surface meteorological variables in the Columbia river gorge and basin during the second wind forecast improvement project, Bound.-Lay. Meteorol., 182, 147–172, https://doi.org/10.1007/s10546-021-00645-x, 2022.

Blay-Carreras, E., Pino, D., Vilà-Guerau De Arellano, J., Van De Boer, A., De Coster, O., Darbieu, C., Hartogensis, O., Lohou, F., Lothon, M., and Pietersen, H.: Role of the residual layer and large-scale subsidence on the development and evolution of the convective boundary layer, Atmos. Chem. Phys., 14, 4515–4530, https://doi.org/10.5194/acp-14-4515-2014, 2014.

Brooks, I. M.: Finding Boundary Layer Top: Application of a wavelet covariance transform to lidar backscatter profiles, J. Atmos. Ocean. Tech., 20, 1092–1105, https://doi.org/10.1175/1520-0426(2003)020<1092:FBLTAO>2.0.CO;2, 2003.

Brooks, I. M. and Fowler, A. M.: A new measure of entrainment zone structure, Geophys. Res. Lett., 34, 2007GL030958, https://doi.org/10.1029/2007GL030958, 2007.

Burgos-Cuevas, A., Adams, D. K., García-Franco, J.L., and Ruiz-Angulo, A.: A seasonal climatology of the Mexico City atmospheric boundary layer, Bound.-Lay. Meteorol., 180, 131–154, https://doi.org/10.1007/s10546-021-00615-3, 2021.

Burgos-Cuevas, A., Magaldi, A., Adams, D. K., Grutter, M., García-Franco, J. L., and Ruiz-Angulo, A.: Boundary layer height characteristics in Mexico City from two remote sensing techniques, Bound.-Lay. Meteorol., 186, 287–304, https://doi.org/10.1007/s10546-022-00759-w, 2023.

Chandra, A. S., Kollias, P., Giangrande, S. E., and Klein, S. A.: Long-term observations of the convective boundary layer using insect radar returns at the SGP ARM climate research facility, J. Climate, 23, 5699–5714, https://doi.org/10.1175/2010JCLI3395.1, 2010.

Clothiaux, E. E., Ackerman, T. P., Mace, G. G., Moran, K. P., Marchand, R. T., Miller, M. A., and Martner, B. E.: Objective determination of cloud heights and radar reflectivities using a combination of active remote sensors at the ARM CART sites, J. Appl. Meteorol., 39, 645–665, https://doi.org/10.1175/1520-0450(2000)039<0645:ODOCHA>2.0.CO;2, 2000.

Dang, R., Yang, Y., Hu, X.-M., Wang, Z., and Zhang, S.: A review of techniques for diagnosing the atmospheric boundary layer height (ABLH) using aerosol lidar data, Remote Sens.-Basel, 11, 1590, https://doi.org/10.3390/rs11131590, 2019.

Davis, K. J., N. Gamage, C. Hagelberg, C. Kiemle, D. Lenschow, and P. Sullivan: An objective method for deriving atmospheric structure from airborne lidar observations, J. Atmos. Ocean. Tech., 17,

1455–1468, doi:10.1175/1520-0426(2000)017<1455:AOMFDA>2.0.CO;2, 2000.

de Arruda Moreira, G., Guerrero-Rascado, J. L., Bravo-Aranda, J. A., Benavent-Oltra, J. A., Ortiz-Amezcua, P., Román, R., Bedoya-Velásquez, A. E., Landulfo, E., and Alados-Arboledas, L.: Study of the planetary boundary layer by microwave radiometer, elastic lidar and Doppler lidar estimations in Southern Iberian Peninsula, Atmos. Res., 213, 185–195, https://doi.org/10.1016/j.atmosres.2018.06.007, 2018.

Dewani, N., Sakradzija, M., Schlemmer, L., Leinweber, R., and Schmidli, J.: Dependency of vertical velocity variance on meteorological conditions in the convective boundary layer, Atmos. Chem. Phys., 23, 4045–4058, https://doi.org/10.5194/acp-23-4045-2023, 2023.

Edwards, J. M., Beljaars, A. C. M., Holtslag, A. A. M., and Lock, A. P.: Representation of boundary-layer processes in numerical weather prediction and climate models, Bound.-Lay. Meteorol., 177, 511–539, https://doi.org/10.1007/s10546-020-00530-z, 2020.

Emeis, S., K. Schäfer, and C. Münkel: Surface-based remote sensing of the mixing-layer height—A review, Meteorol. Z., 17, 621–630, https://doi.org/10.1127/0941-2948/2008/0312, 2008.

Fang, J., Huang, K., Du, M., Zhang, Z., Cao, R., and Yi, F.: Investigation on cloud vertical structures based on Ka-band cloud radar observations at Wuhan in Central China, Atmos. Res., 281, 106492, https://doi.org/10.1016/j.atmosres.2022.106492, 2023.

Fernald, F. G.: Analysis of atmospheric lidar observations: Some comments, Appl. Opt., 23, 652–653, https://doi.org/10.1364/AO.23.000652, 1984.

Franck, A., Moisseev, D., Vakkari, V., Leskinen, M., Lampilahti, J., Kerminen, V.-M., and O'Connor, E.: Evaluation of convective boundary layer height estimates using radars operating at different frequency bands, Atmos. Meas. Tech., 14, 7341–7353, https://doi.org/10.5194/amt-14-7341-2021, 2021.

Freudenthaler, V., Esselborn, M., Wiegner, M., Heese, B., Tesche, M., Ansmann, A., Müller, D., Althausen,

528 D., Wirth, M., Fix, A., Ehret, G., Knippertz, P., Toledano, C., Gasteiger, J., Garhammer, M., and
529 Seefeldner, M.: Depolarization ratio profiling at several wavelengths in pure Saharan dust during
530 SAMUM 2006, Tellus B, 61, 165, https://doi.org/10.1111/j.1600-0889.2008.00396.x, 2009.
531 Görsdorf, U., Lehmann, V., Bauer-Pfundstein, M., Peters, G., Vavriv, D., Vinogradov, V., and Volkov, V.: A
532 35-GHz polarimetric doppler radar for long-term observations of cloud parameters—description of
533 system and data processing, J. Atmos. Ocean. Tech., 32, 675–690,
534 https://doi.org/10.1175/JTECH-D-14-00066.1, 2015.
535 Granados-Muñoz, M. J., Navas-Guzmán, F., Bravo-Aranda, J. A., Guerrero-Rascado, J. L., Lyamani, H.,
536 Fernández-Gálvez, J., and Alados-Arboledas, L.: Automatic determination of the planetary boundary
537 layer height using lidar: One-year analysis over southeastern Spain, J. Geophys. Res.-Atmos., 117,
538 https://doi.org/10.1029/2012JD017524, 2012.
539 Grossman and Robert, L.: Observed effects of horizontal radiative surface temperature variations on the
540 atmosphere over a midwest watershed during CASES 97, J. Geophys. Res.-Atmos., 110,
541 https://doi.org/10.1029/2004JD004542, 2005.
542 Guo, J., Miao, Y., Zhang, Y., Liu, H., Li, Z., Zhang,W., He, J., Lou, M., Yan, Y., Bian, L., and Zhai, P.: The
543 climatology of planetary boundary layer height in China derived from radiosonde and reanalysis data,
544 Atmos. Chem. Phys., 16, 13309–13319, https://doi.org/10.5194/acp-16-13309-2016, 2016.
545 Guo, J., Su, T., Li, Z., Miao, Y., Li, J., Liu, H., Xu, H., Cribb, M., and Zhai, P.: Declining frequency of
546 summertime local-scale precipitation over eastern China from 1970 to 2010 and its potential link to
547 aerosols, Geophys. Res. Lett., 44, 5700–5708, https://doi.org/10.1002/2017GL073533, 2017.
548 Guo, J., Zhang, J., Yang, K., Liao, H., Zhang, S., Huang, K., Lv, Y., Shao, J., Yu, T., Tong, B., Li, J., Su, T.,
549 Yim, S. H. L., Stoffelen, A., Zhai, P., and Xu, X.: Investigation of near-global daytime boundary layer
550 height using high-resolution radiosondes: first results and comparison with ERA5, MERRA-2, JRA-55,

551 and NCEP-2 reanalyses, Atmos. Chem. Phys., 21, 17079–17097,
552 https://doi.org/10.5194/acp-21-17079-2021, 2021.
553 Guo, X., Huang, K., Fang, J., Zhang, Z., Cao, R., Yi, F.: Seasonal and diurnal changes of air temperature and
554 water vapor observed with a microwave radiometer in Wuhan, China, Remote Sens.-Basel, 15, 5422.
555 https://doi.org/10.3390/rs15225422, 2023.
556 Heus, T., Van Heerwaarden, C. C., Jonker, H. J. J., Pier Siebesma, A., Axelsen, S., Van Den Dries, K.,
557 Geoffroy, O., Moene, A. F., Pino, D., De Roode, S. R., and Vilà-Guerau De Arellano, J.: Formulation of
558 the Dutch Atmospheric Large-Eddy Simulation (DALES) and overview of its applications, Geosci.
559 Model Dev., 3, 415–444, https://doi.org/10.5194/gmd-3-415-2010, 2010.
560 Holtslag, A. A. M. and Nieuwstadt, F. T. M.: Scaling the atmospheric boundary layer, Bound.-Lay. Meteorol.,
561 36, 201–209, https://doi.org/10.1007/BF00117468, 1986.
562 Huang, M., Gao, Z., Miao, S., Chen, F., LeMone, M. A., Li, J., Hu, F., and Wang, L.: Estimate of
563 boundary-layer depth over Beijing, China, using doppler lidar data during SURF-2015, Bound.-Lay.
564 Meteorol., 162, 503–522, https://doi.org/10.1007/s10546-016-0205-2, 2017.
565 Immler, F. and Schrems, O.: Vertical profiles, optical and microphysical properties of Saharan dust layers
566 determined by a ship-borne lidar, Atmos. Chem. Phys., https://doi.org/10.5194/acp-3-1353-2003, 2003.
567 Klett, J. D.: Stable analytical inversion solution for processing lidar returns, Appl. Opt., 20, 211–220,
568 https://doi.org/10.1364/AO.20.000211, 1981.
569 Kong, W. and Yi, F.: Convective boundary layer evolution from lidar backscatter and its relationship with
570 surface aerosol concentration at a location of a central China megacity, J. Geophys. Res.-Atmos., 120,
571 7928–7940, https://doi.org/10.1002/2015JD023248, 2015.
572 Kotthaus, S., Bravo-Aranda, J. A., Collaud Coen, M., Guerrero-Rascado, J. L., Costa, M. J., Cimini, D.,
573 O'Connor, E. J., Hervo, M., Alados-Arboledas, L., Jiménez-Portaz, M., Mona, L., Ruffieux, D.,

574 Illingworth, A., and Haeffelin, M.: Atmospheric boundary layer height from ground-based remote
575 sensing: a review of capabilities and limitations, Atmos. Meas. Tech., 16, 433–479,
576 https://doi.org/10.5194/amt-16-433-2023, 2023.
577 Kwon, H.-G., Yang, H., and Yi, C.: Study on radiative flux of road resolution during winter based on local
578 weather and topography, Remote Sens.-Basel, 14, 6379, https://doi.org/10.3390/rs14246379, 2022.
579 Lammert, A. and Bösenberg, J.: Determination of the convective boundary-layer height with laser remote
580 sensing, Bound.-Lay. Meteorol., 119, 159–170, https://doi.org/10.1007/s10546-005-9020-x, 2006.
581 LeMone, M. A., Chen, F., Tewari, M., Dudhia, J., Geerts, B., Miao, Q., Coulter, R. L., and Grossman, R. L.:
582 Simulating the IHOP_2002 fair-weather CBL with the WRF-ARW–Noah modeling system. Part I:
583 Surface fluxes and CBL structure and evolution along the eastern track, Mon. Weather Rev., 138,
584 722–744, https://doi.org/10.1175/2009MWR3003.1, 2010.
585 Lewis, J., E. J. Welton, A. M. Molod, and E. Joseph: Improved boundary layer depth retrievals from
586 MPLNET, J. Geophys. Res.-Atmos., 118, 9870–9879, https://doi.org/10.1002/jgrd.50570, 2013.
587 Li, H., Yang, Y., Hu, X., Huang, Z., Wang, G., Zhang, B., and Zhang, T.: Evaluation of retrieval methods of
588 daytime convective boundary layer height based on lidar data, J. Geophys. Res.-Atmos., 122,
589 4578–4593, https://doi.org/10.1002/2016JD025620, 2017.
590 Liu, B., Ma, Y., Guo, J., Gong, W., Zhang, Y., Mao, F., Li, J., Guo, X., and Shi, Y.: Boundary layer heights as
591 derived from ground-based radar wind profiler in Beijing, IEEE T. Geosci. Remote, 57, 8095–8104,
592 https://doi.org/10.1109/TGRS.2019.2918301, 2019.
593 Liu, F., Yi, F., Yin, Z., Zhang, Y., He, Y., and Yi, Y.: Measurement report: characteristics of clear-day
594 convective boundary layer and associated entrainment zone as observed by a ground-based polarization
595 lidar over Wuhan (30.5° N, 114.4° E), Atmos. Chem. Phys., 21, 2981–2998,
596 https://doi.org/10.5194/acp-21-2981-2021, 2021.

Liu, S. and Liang, X.-Z.: Observed diurnal cycle climatology of planetary boundary layer height, J. Climate, 23, 5790–5809, https://doi.org/10.1175/2010JCLI3552.1, 2010.

Mahrt, L.: Stratified atmospheric boundary layers, Bound.-Lay. Meteorol., 90, 375–396, https://doi.org/10.1023/A:1001765727956, 1999.

Manninen, A. J., Marke, T., Tuononen, M., and O'Connor, E. J.: Atmospheric boundary layer classification with doppler lidar, J. Geophys. Res.-Atmos., 123, 8172–8189, https://doi.org/10.1029/2017JD028169, 2018.

Mao, Z., Huang, K., Fang, J., Zhang, Z., Cao, R., and Yi, F.: An Observation of precipitation during cooling with Ka-Band cloud radar in Wuhan, China, Remote Sens.-Basel, 15, 5397, https://doi.org/10.3390/rs15225397, 2023.

Martucci, G., R. Matthey, V. Mitev, and H. Richner: Comparison between backscatter lidar and radiosonde measurements of the diurnal and nocturnal stratification in the lower troposphere, J. Atmos. Ocean. Tech., 24, 1231–1244, https://doi.org/10.1175/JTECH2036.1, 2007.

Moran, K. P., Martner, B. E., Post, M. J., Kropfli, R. A., Welsh, D. C., and Widener, K. B.: An unattended cloud-profiling radar for use in climate research, B. Am. Meteorol. Soc., 79, 443–455, https://doi.org/10.1175/1520-0477(1998)079<0443:AUCPRF>2.0.CO;2, 1998.

Neggers, R. A. J., Siebesma, A. P., Lenderink, G., and Holtslag, A. A. M.: An evaluation of mass flux closures for diurnal cycles of shallow cumulus, Mon. Weather Rev., 132, 2525–2538, https://doi.org/10.1175/MWR2776.1, 2004.

Pal, S., Behrendt, A., and Wulfmeyer, V.: Elastic-backscatter-lidar-based characterization of the convective boundary layer and investigation of related statistics, Ann. Geophys.-Italy, 28, 825–847, https://doi.org/10.5194/angeo-28-825-2010, 2010.

Pal, S., Lopez, M., Schmidt, M., Ramonet, M., Gibert, F., Xueref-Remy, I., and Ciais, P.: Investigation of the

620 atmospheric boundary layer depth variability and its impact on the 222 Rn concentration at a rural site
621 in France, J. Geophys. Res.-Atmos., 120, 623–643, https://doi.org/10.1002/2014JD022322, 2015.
622 Pearson, G., Davies, F., and Collier, C.: Remote sensing of the tropical rain forest boundary layer using
623 pulsed Doppler lidar, Atmos. Chem. Phys., 10, 5891–5901, https://doi.org/10.5194/acp-10-5891-2010,
624 2010.
625 Piironen, A. K. and Eloranta, E. W.: Convective boundary layer mean depths and cloud geometrical
626 properties obtained from volume imaging lidar data, J. Geophys. Res.-Atmos., 100, 25569–25576,
627 https://doi.org/10.1029/94JD02604, 1995.
628 Ribeiro, F. N. D., Oliveira, A. P. D., Soares, J., Miranda, R. M. D., Barlage, M., and Chen, F.: Effect of sea
629 breeze propagation on the urban boundary layer of the metropolitan region of Sao Paulo, Brazil, Atmos.
630 Res., 214, 174–188, https://doi.org/10.1016/j.atmosres.2018.07.015, 2018.
631 Sandeep, A., Rao, T. N., Ramkiran, C. N., and Rao, S. V. B.: Differences in atmospheric boundary-layer
632 characteristics between wet and dry episodes of the Indian summer monsoon, Bound.-Lay. Meteorol.,
633 153, 217–236, https://doi.org/10.1007/s10546-014-9945-z, 2014.
634 Schneider, S. P.: Effects of roughness on hypersonic boundary-layer transition, J. Spacecraft Rockets, 45,
635 193–209, https://doi.org/10.2514/1.29713, 2008.
636 Schween, J. H., Hirsikko, A., Löhnert, U., and Crewell, S.: Mixing-layer height retrieval with ceilometer and
637 Doppler lidar: from case studies to long-term assessment, Atmos. Meas. Tech., 7, 3685–3704,
638 https://doi.org/10.5194/amt-7-3685-2014, 2014.
639 Seibert, P.: Review and intercomparison of operational methods for the determination of the mixing height,
640 Atmos. Environ., 34, 1001–1027, https://doi.org/10.1016/S1352-2310(99)00349-0, 2000.
641 Seidel, D. J., Ao, C. O., and Li, K.: Estimating climatological planetary boundary layer heights from
642 radiosonde observations: Comparison of methods and uncertainty analysis, J. Geophys. Res.-Atmos.,

115, 2009JD013680, https://doi.org/10.1029/2009JD013680, 2010.

Seidel, D. J., Zhang, Y., Beljaars, A., Golaz, J., Jacobson, A. R., and Medeiros, B.: Climatology of the planetary boundary layer over the continental United States and Europe, J. Geophys. Res.-Atmos., 117, 2012JD018143, https://doi.org/10.1029/2012JD018143, 2012.

Singh, N., Solanki, R., Ojha, N., Janssen, R. H. H., Pozzer, A., and Dhaka, S. K.: Boundary layer evolution over the central Himalayas from radio wind profiler and model simulations, Atmos. Chem. Phys., 16, 10559–10572, https://doi.org/10.5194/acp-16-10559-2016, 2016.

Solanki, R., Guo, J., Li, J., Singh, N., Guo, X., Han, Y., Lv, Y., Zhang, J., and Liu, B.: Atmospheric-boundary-layer-height variation over mountainous and urban sites in Beijing as derived from radar wind-profiler measurements, Bound.-Lay. Meteorol., 181, 125–144, https://doi.org/10.1007/s10546-021-00639-9, 2021.

Stull, R. B.: An Introduction to Boundary Layer Meteorology, Springer Netherlands, Dordrecht, https://doi.org/10.1007/978-94-009-3027-8, 1988.

Su, T., Li, Z., and Kahn, R.: A new method to retrieve the diurnal variability of planetary boundary layer height from lidar under different thermodynamic stability conditions, Remote Sens.-Basel Environ., 237, 111519, https://doi.org/10.1016/j.rse.2019.111519, 2020.

Tang, G., Zhang, J., Zhu, X., Song, T., Münkel, C., Hu, B., Schäfer, K., Liu, Z., Zhang, J., Wang, L., Xin, J., Suppan, P., and Wang, Y.: Mixing layer height and its implications for air pollution over Beijing, China, Atmos. Chem. Phys., 16, 2459–2475, https://doi.org/10.5194/acp-16-2459-2016, 2016.

Tennekes, H. and Driedonks, A. G. M.: Basic entrainment equations for the atmospheric boundary layer, Bound.-Lay. Meteorol., 20, 515–531, https://doi.org/10.1007/BF00122299, 1981.

Träumner, K., Kottmeier, C., Corsmeier, U., and Wieser, A.: Convective boundary-layer entrainment: short review and progress using doppler lidar, Bound.-Lay. Meteorol., 141, 369–391,

https://doi.org/10.1007/s10546-011-9657-6, 2011.

Tucker, S. C., Senff, C. J., Weickmann, A. M., Brewer, W. A., Banta, R. M., Sandberg, S. P., Law, D. C., and Hardesty, R. M.: Doppler lidar estimation of mixing height using turbulence, shear, and aerosol profiles, J. Atmos. Ocean. Tech., 26, 673–688, https://doi.org/10.1175/2008JTECHA1157.1, 2009.

Van Der Kamp, D. and McKendry, I.: Diurnal and seasonal trends in convective mixed-layer heights estimated from two years of continuous ceilometer observations in Vancouver, BC, Bound.-Lay. Meteorol., 137, 459–475, https://doi.org/10.1007/s10546-010-9535-7, 2010.

Yang, T., Wang, Z., Zhang, W., Gbaguidi, A., Sugimoto, N., Wang, X., Matsui, I., and Sun, Y.: Technical note: Boundary layer height determination from lidar for improving air pollution episode modeling: development of new algorithm and evaluation, Atmos. Chem. Phys., 17, 6215–6225, https://doi.org/10.5194/acp-17-6215-2017, 2017.

Yates, D. N., Chen, F., Lemone, M. A., Qualls, R., Oncley, S. P., and Gross, R. L.: A cooperative atmosphere-surface exchange study (CASES) dataset for analyzing and parameterizing the effects of land surface heterogeneity on area-averaged surface heat fluxes, J. Appl. Meteorol., 40, https://doi.org/10.1175/1520-0450(2001)040<0921:ACASES>2.0.CO;2, 2001.

Zhang, H., Zhou, X., Zou, J., Wang, W., Xue, L., Ding, Q., Wang, X., Zhang, N., Ding, A., Sun, J., and Wang, W.: A review on the methods for observing the substance and energy exchange between atmosphere boundary layer and free troposphere, Remote Sens.-Basel, 15, 5397, https://doi.org/10.3390/rs15225397, 2018.

Zhang, J., Guo, J., Li, J., Zhang, S., Tong, B., Shao, J., Li, H., Zhang, Y., Cao, L., Zhai, P., Xu, X., and Wang, M.: A Climatology of merged daytime planetary boundary layer height over China from radiosonde measurements, J. Geophys. Res.-Atmos., 127, e2021JD036367, https://doi.org/10.1029/2021JD036367,

2022.

Zhang, M., Tian, P., Zeng, H., Wang, L., Liang, J., Cao, X., and Zhang, L.: A comparison of wintertime atmospheric boundary layer heights determined by tethered balloon soundings and lidar at the site of SACOL, Remote Sens.-Basel, 13, 1781, https://doi.org/10.3390/rs13091781, 2021.

Zhang, Y., Zhang, S., Huang, C., Huang, K., Gong, Y., and Gan, Q.: Diurnal variations of the planetary boundary layer height estimated from intensive radiosonde observations over Yichang, China, Sci. China Technol. Sc., 57, 2172–2176, https://doi.org/10.1007/s11431-014-5639-5, 2014.

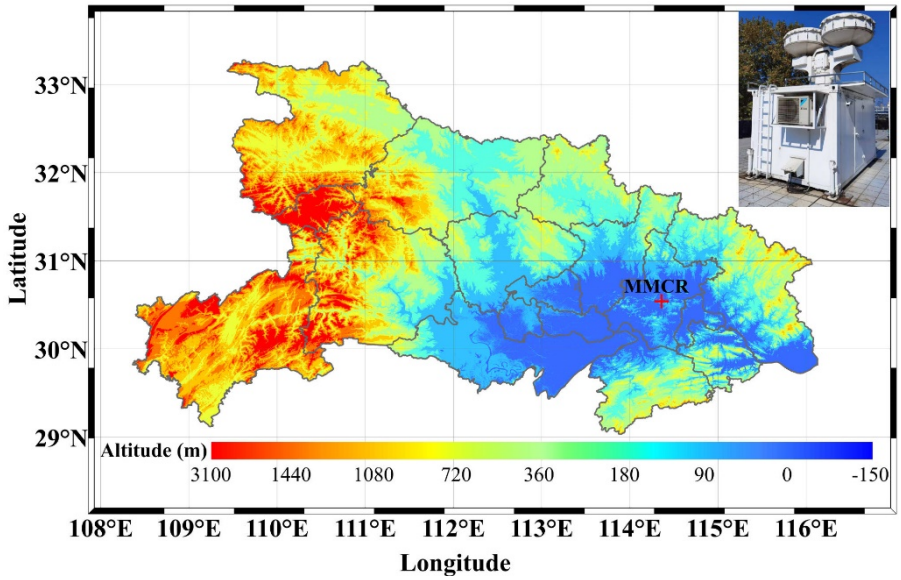

Figure 1. Topographic elevation map of Hubei Province and Ka-band MMCR located in Wuhan University (30.54°N, 114.36°E). The red crisscross denotes the site of MMCR.

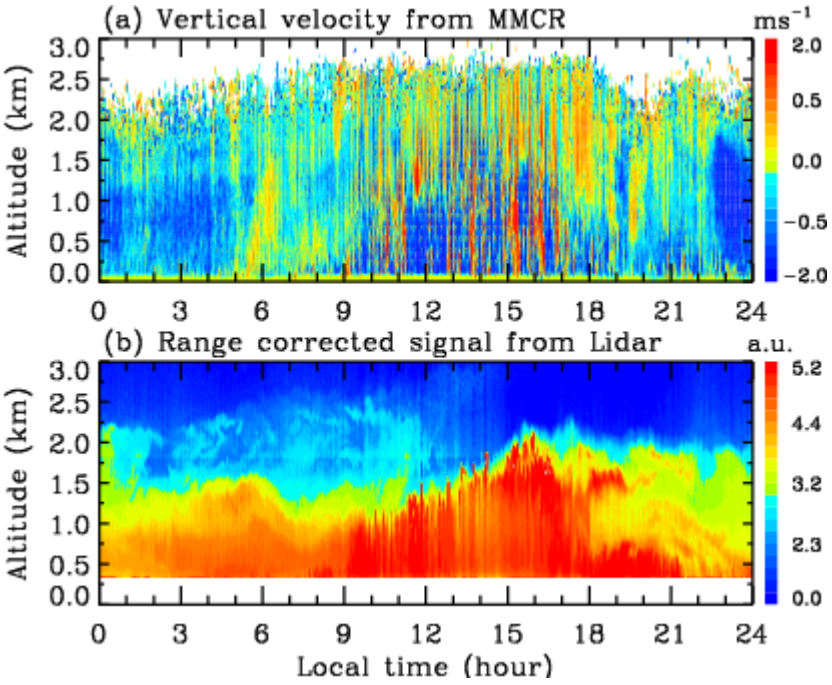

698

699 **Figure 2.** Time-height section of (a) vertical velocity from MMCR and (b) RCS from lidar on 15 August

700 2020.

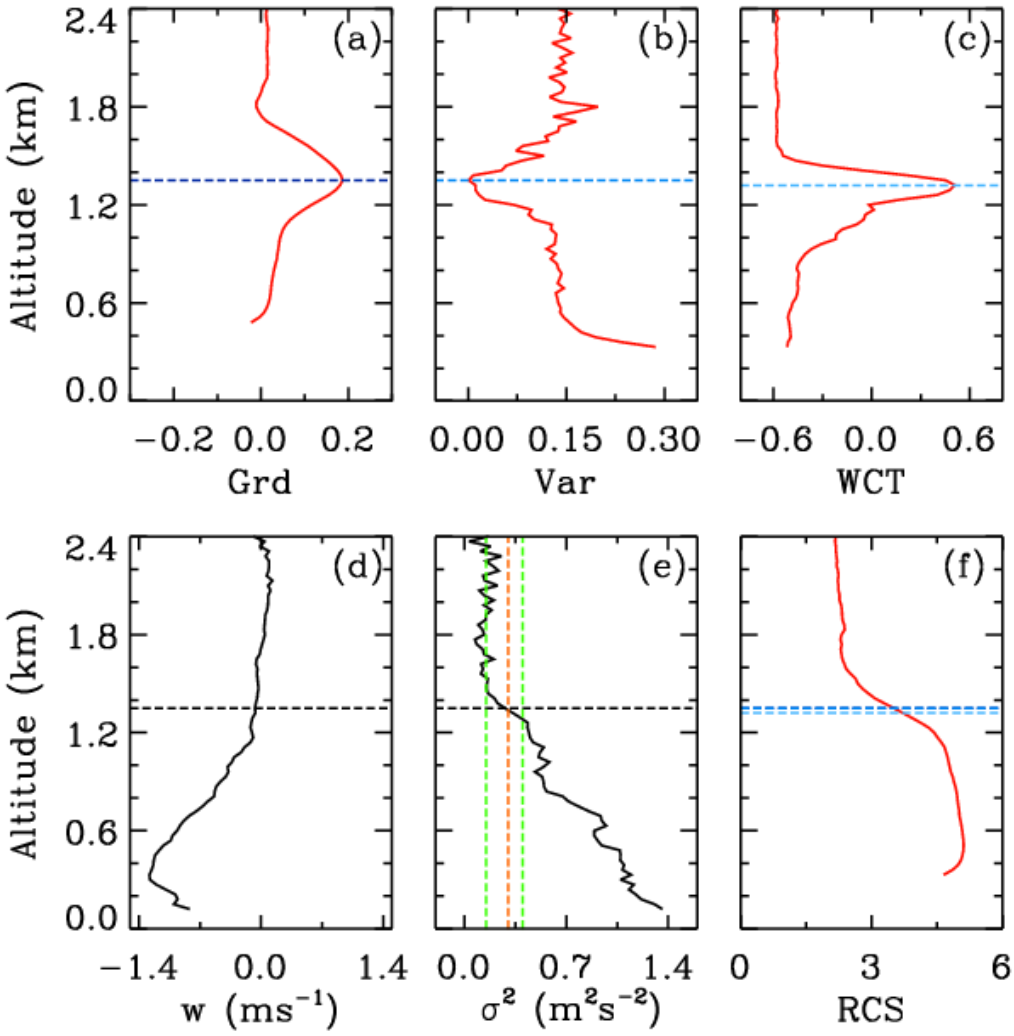

701

702 **Figure 3.** Profiles of (a) RCS gradient, (b) variance, (c) WCT and (f) RCS form lidar, and (d) vertical

703 velocity and (e) its variance from MMCR between 12:15 and 12:45 LT on 15 August 2020. In these panels,

704 the horizontal lines in different colors represent the CBLH determined by different methods. In Panel 3e, the

705 orange vertical line denotes the selected threshold of 0.3 $m^2 s^{-2}$, and the two green vertical lines correspond

706 to the variances of 0.15 and 0.4 $m^2 s^{-2}$, respectively.

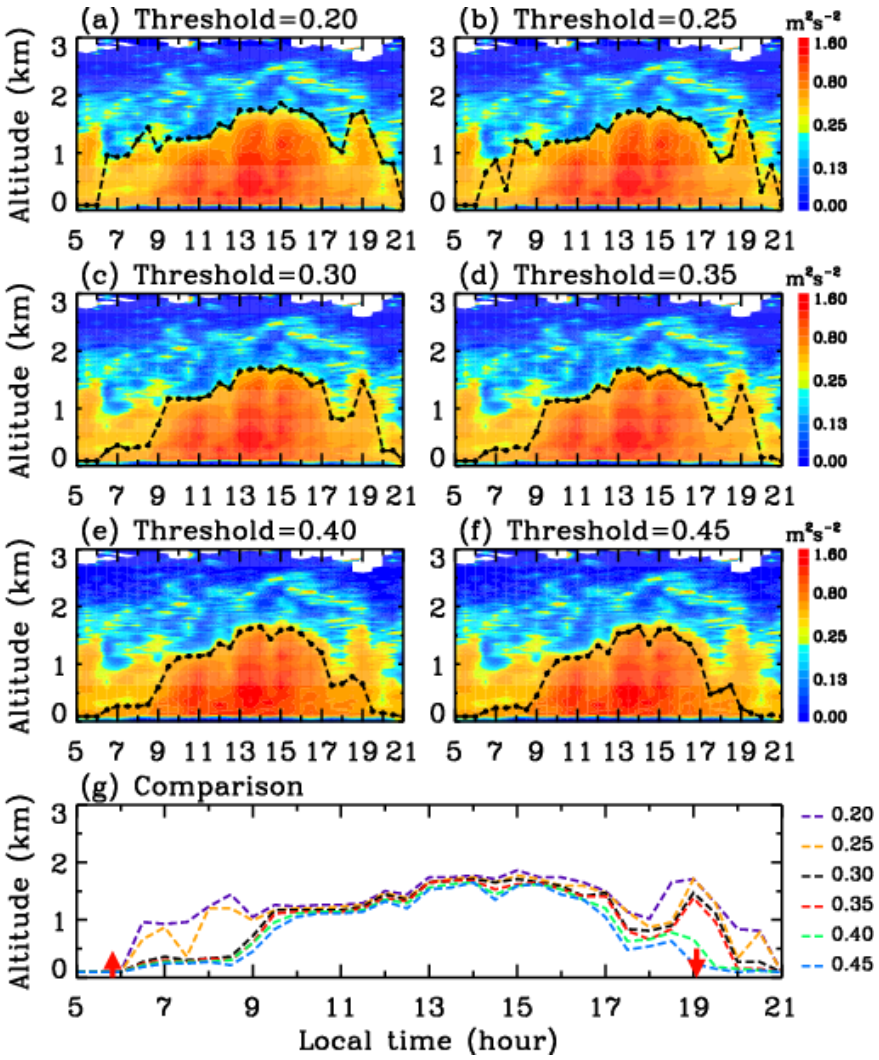

Figure 4. CBLHs derived from thresholds of (a) 0.2, (b) 0.25, (c) 0.3, (d) 0.35, (e) 0.4 and (f) 0.45 $m^2 s^{-2}$ superimposed over vertical velocity variance (color shading) from MMCR on 15 August 2020, and (g) their comparison. In Panel 4g, the two red arrows denote the time of sunrise and sunset at 05:50 and 19:05, respectively.

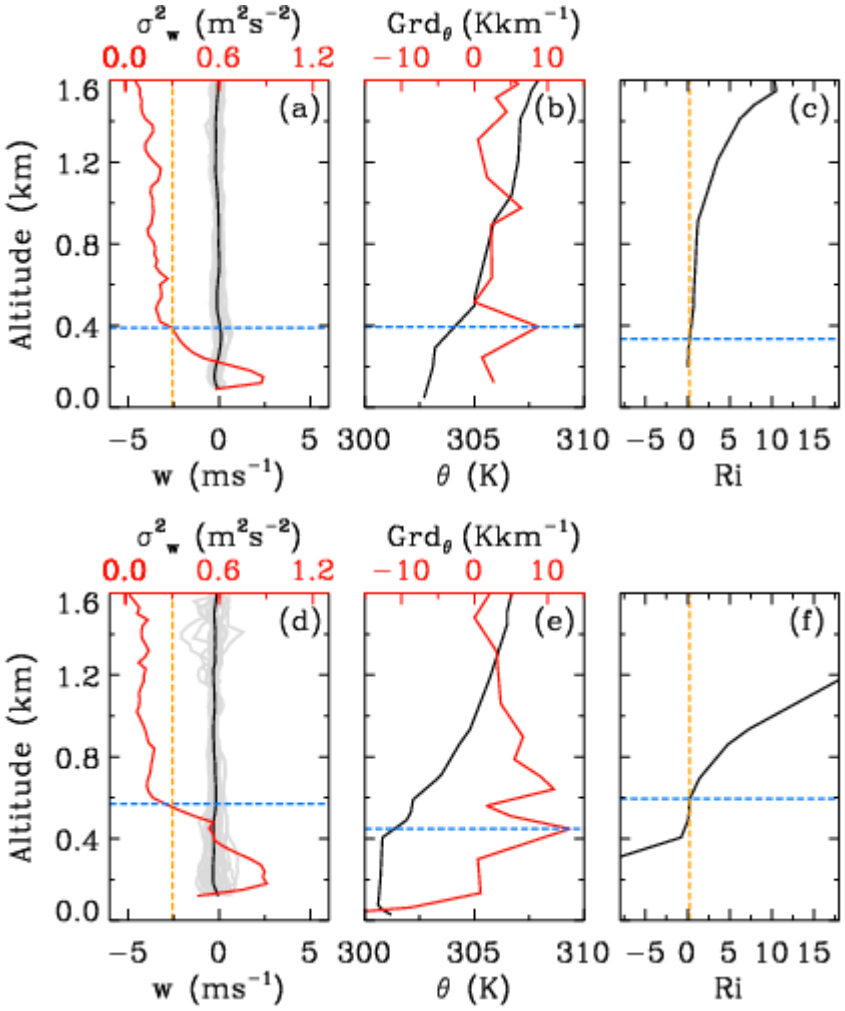

713

714 **Figure 5.** Comparison of CBLHs estimated by (a, d) threshold of σ_w^2=0.3 m^2 s^{-2} from MMCR, and (b, e)
715 maximum gradient of θ and (c, f) threshold of Ri=0.25 from radiosonde data at 08:00 on (upper) 21 and
716 (lower) 25 July 2021. In the panels 5a and 5d, the gray and black lines denote (lower horizontal axis) w and its
717 mean value from MMCR, respectively, and the red and yellow lines denote (upper horizontal axis) σ_w^2 and the
718 threshold of σ_w^2=0.3 m^2 s^{-2}, respectively. In the panels 5b and 5e, the black and red lines denote (lower
719 horizontal axis) θ and (upper horizontal axis) its gradient from radiosonde, respectively. In the panels 5c and
720 5f, the black and yellow lines denote Ri and the threshold of Ri=0.25 from radiosonde data, respectively.
721 The blue horizontal line represents the position of identified CBL top.

722

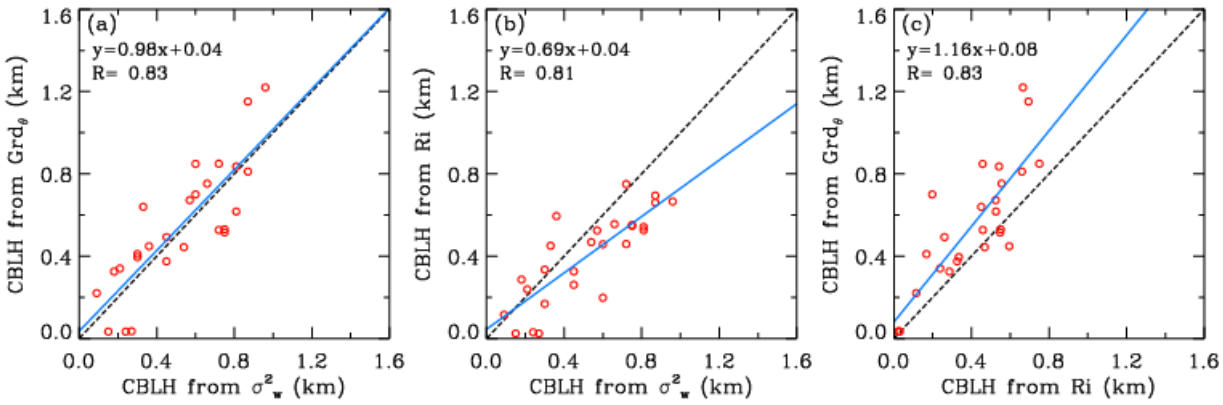

723

724 **Figure 6.** Scatterplot of CBLHs derived from (a) threshold of σ_w^2=0.3 m^2 s^{-2} from MMCR vs. maximum

725 gradient of θ from radiosonde, (b) threshold of σ_w^2=0.3 m^2 s^{-2} from MMCR vs. threshold of Ri=0.25 from

726 radiosonde, and (c) threshold of Ri=0.25 vs. maximum gradient of θ from radiosonde.

727

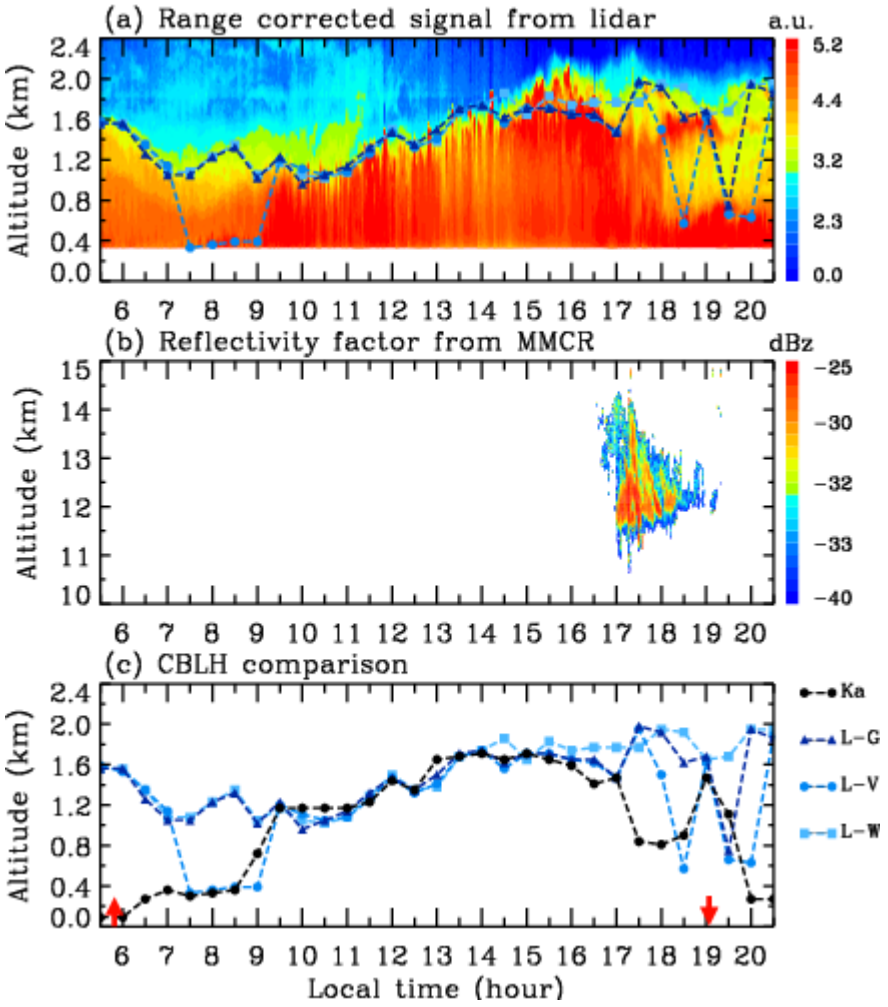

728

729 **Figure 7.** (a) Evolution of CBLH derived from RCS gradient, variance and WCT superimposed over lidar

730 RCS (color shading) on 15 August 2020, (b) reflectivity factor from MMCR, and (c) comparison of CBLHs

731 derived from MMCR and lidar observations. The black dash curve with circle (Ka) denotes the CBLH

732 determined by the variance threshold of 0.3 $m^2 s^{-2}$ in the Ka-band MMCR observation, while the dark blue,

733 blue and light blue dash curves with triangle (L-G), circle (L-V) and square (L-W) represent the CBLH

734 determined by the gradient, variance and WCT in the lidar measurement, respectively. In Panel 5c, the two

735 red arrows denote the time of sunrise and sunset at 05:50 and 19:05, respectively.

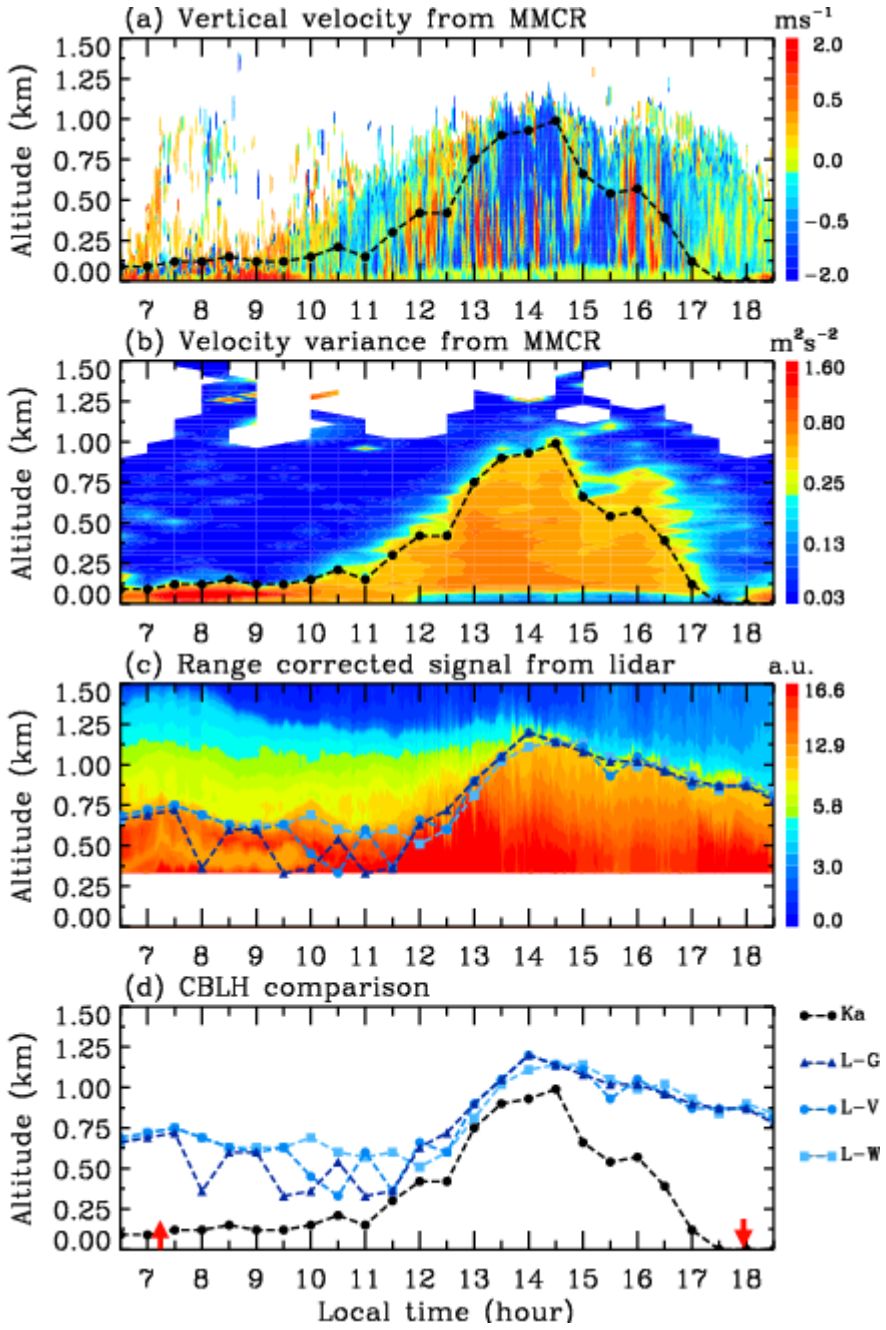

736

737 **Figure 8.** Distributions of (a) vertical velocity and (b) its variance from MMCR and (c) lidar RCS on 31

738 January 2020 with retrieved CBLH, and (d) comparison of CBLHs derived from MMCR and lidar

739 observations. The threshold of vertical velocity variance from the MMCR is 0.3 $m^2 s^{-2}$. In Panel 6d, the two

740 red arrows denote the time of sunrise and sunset at 07:15 and 17:57, respectively.

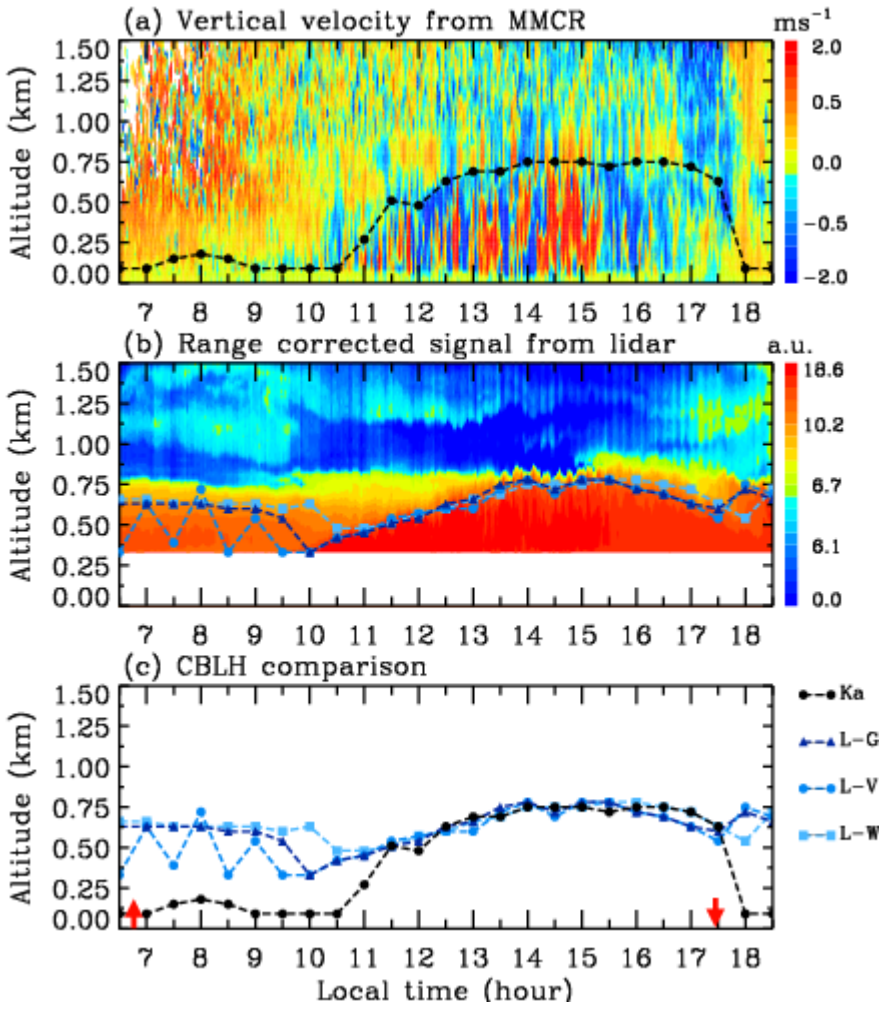

741

742 **Figure 9.** Distributions of (a) vertical velocity from MMCR and (b) lidar RCS on 12 November 2020 with

743 retrieved CBLH, and (c) comparison of CBLHs derived from MMCR and lidar observations. The threshold

744 of vertical velocity variance from the MMCR is 0.3 $m^2 s^{-2}$. In Panel 7c, the two red arrows denote the time of

745 sunrise and sunset at 06:47 and 17:27, respectively.

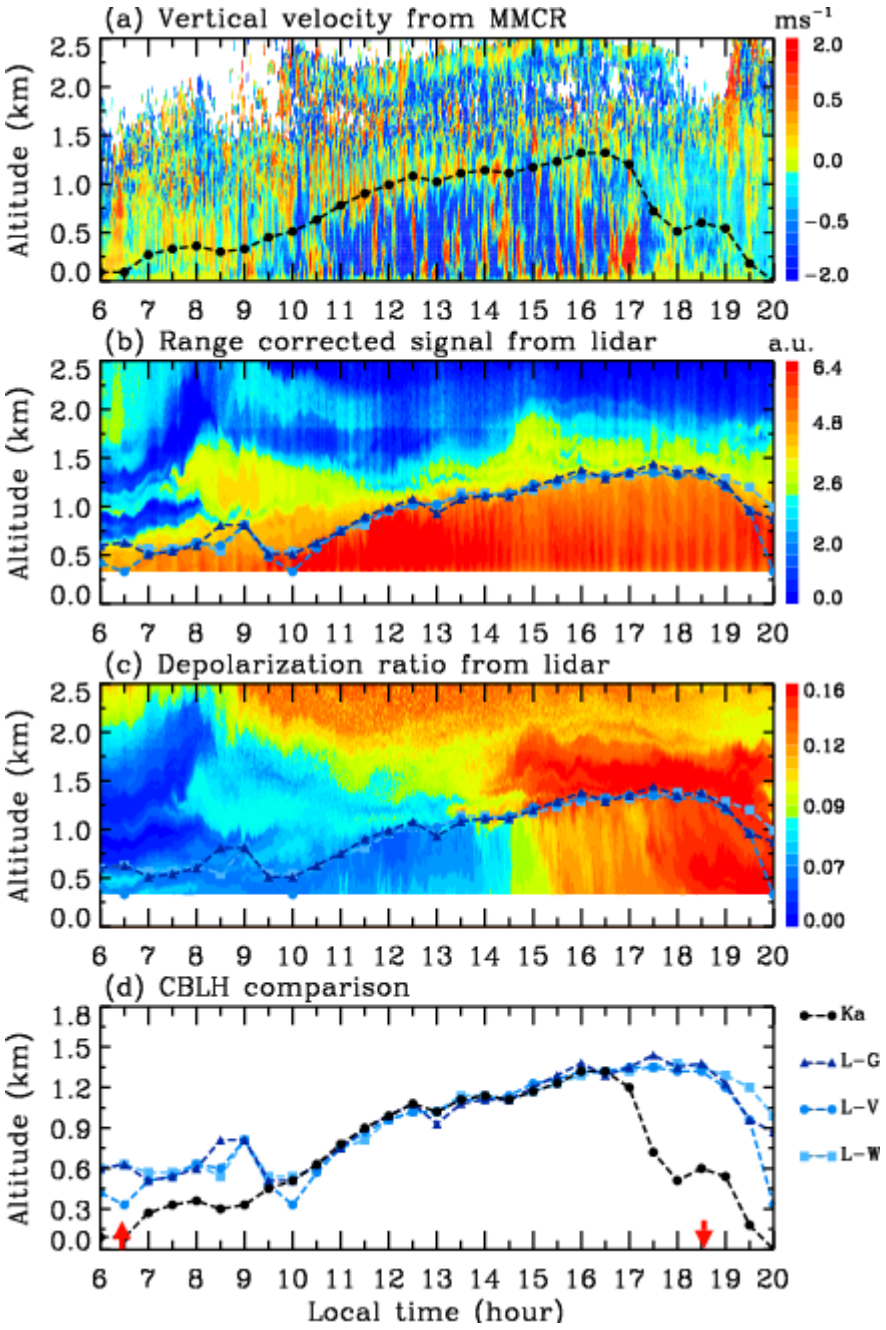

746

747 **Figure 10.** Distributions of (a) vertical velocity from MMCR and lidar (b) RCS and (c) depolarization ratio

748 on 19 March 2020 with retrieved CBLH, and (d) comparison of CBLHs derived from MMCR and lidar

749 observations. The threshold of vertical velocity variance from the MMCR is 0.3 $m^2 s^{-2}$. In Panel 8d, the two

750 red arrows denote the time of sunrise and sunset at 06:27 and 18:34, respectively.

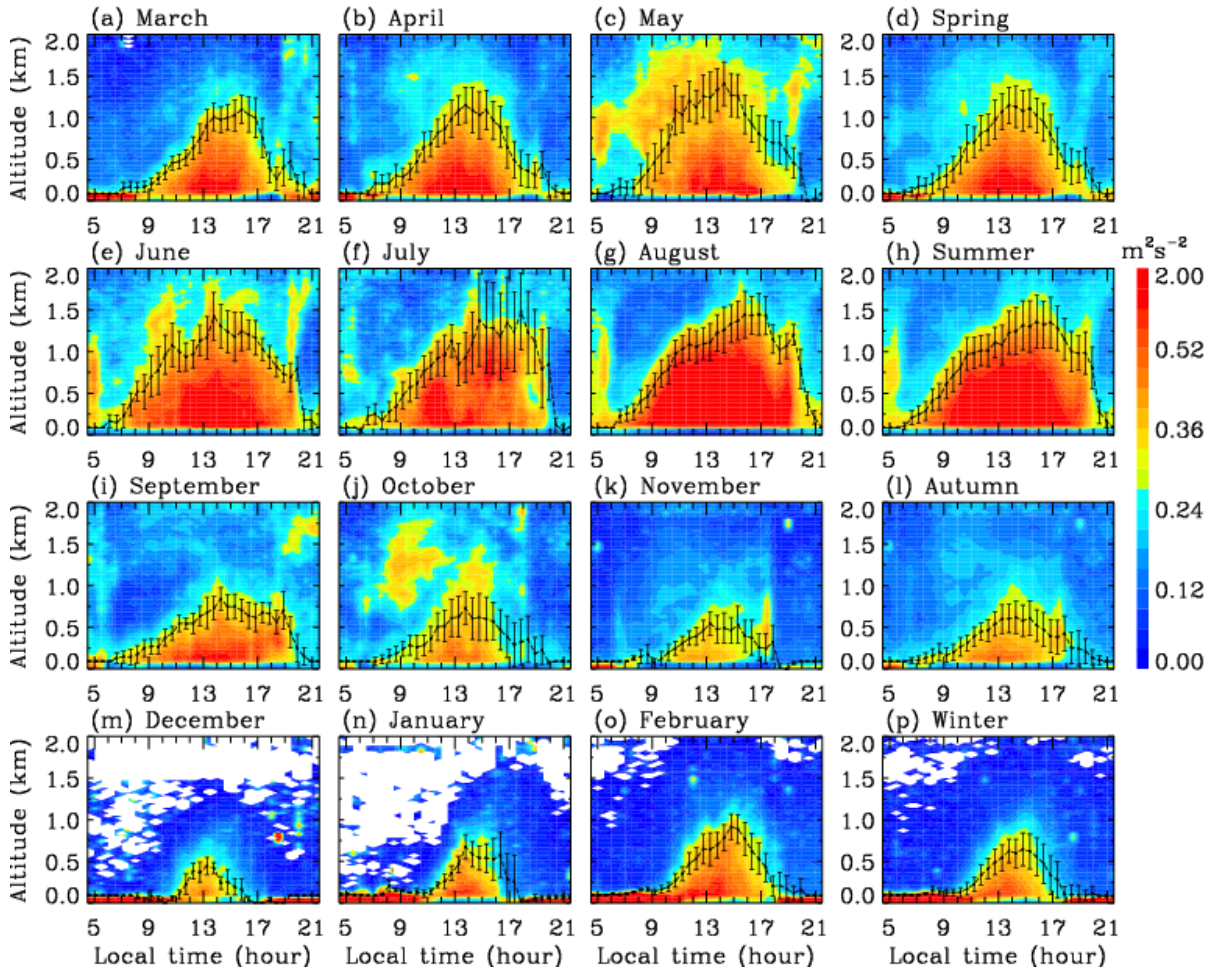

751

752 **Figure 11.** Monthly and seasonal mean values and statistical standard deviations of CBLH estimated by
753 threshold of vertical velocity variance from MMCR. The variance threshold is 0.3 $m^2 s^{-2}$, and the color shading
754 denotes the variance distribution. The months and seasons are marked above the corresponding panels,
755 respectively.